

RESEARCH ARTICLE | APRIL 29 2024

A three-probe method for accurate nanoscale thermal transport measurements

Po-Yen Huang; Tzu-Kan Hsiao ; Jiun-Hung Yi ; Bo-Yi Chen; Yu-Cheng Chiu ; I-Ling Chang ; Tien-Kan Chung ; Ming-Chang Lu  ; Chih-Wei Chang  

 Check for updates

Appl. Phys. Lett. 124, 182201 (2024)

<https://doi.org/10.1063/5.0201873>

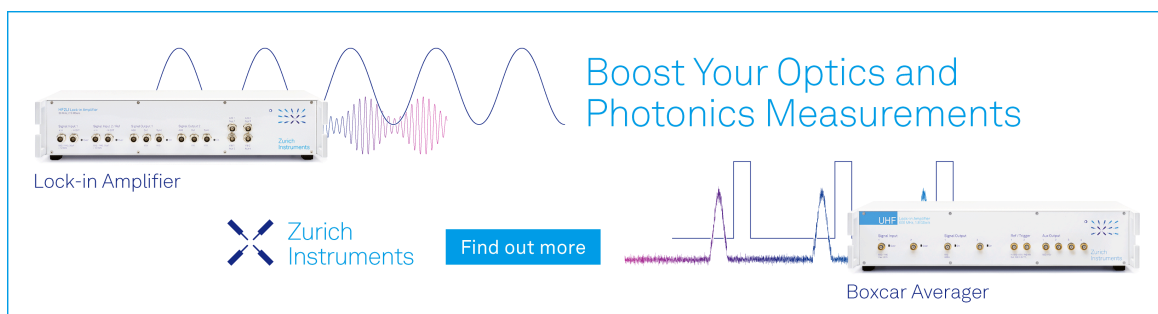


View Online



Export Citation

29 April 2024 10:34:37



Boost Your Optics and Photonics Measurements

Lock-in Amplifier

 Zurich Instruments

[Find out more](#)

Boxcar Averager

A three-probe method for accurate nanoscale thermal transport measurements

Cite as: Appl. Phys. Lett. **124**, 182201 (2024); doi: [10.1063/5.0201873](https://doi.org/10.1063/5.0201873)

Submitted: 1 February 2024 · Accepted: 16 April 2024 ·

Published Online: 29 April 2024



View Online



Export Citation



CrossMark

Po-Yen Huang,^{1,2} Tzu-Kan Hsiao,³ Jiun-Hung Yi,² Bo-Yi Chen,¹ Yu-Cheng Chiu,^{1,4} I-Ling Chang,⁴ Tien-Kan Chung,⁵ Ming-Chang Lu,^{2,6,a)} and Chih-Wei Chang^{1,7,a)}

AFFILIATIONS

¹Center for Condensed Matter Sciences, National Taiwan University, Taipei 10617, Taiwan

²Department of Mechanical Engineering, National Taiwan University, Taiwan 10617, Taiwan

³Department of Physics, National Tsing Hua University, Hsinchu 30013, Taiwan

⁴Department of Mechanical Engineering, National Cheng Kung University, Tainan 70101, Taiwan

⁵Department of Mechanical Engineering, National Yang Ming Chiao Tung University, Hsinchu 30010, Taiwan

⁶Graduate School of Advanced Technology, National Taiwan University, Taipei 10617, Taiwan

⁷Center of Atomic Initiative for New Materials, National Taiwan University, Taipei 10617, Taiwan

^{a)}Authors to whom correspondence should be addressed: mingchangu@ntu.edu.tw and cwchang137@ntu.edu.tw

ABSTRACT

Measurements of transport phenomena are constantly plagued by contact resistance, prohibiting the sample's intrinsic electrical or thermal conductivity from being accurately determined. This predicament is particularly severe in thermal transport measurements due to the inability to meet similar impedance requirements for a four-probe method used in electrical resistance measurements. Here, we invent a three-probe measurement method that makes an accurate determination of thermal conductivity possible for nanomaterials. Incorporating electron beam heating provided by a scanning electron microscope (SEM) on a diffusive thermal conductor not only quantifies the thermal contact resistance, which may introduce an error of more than 270% to a sample's thermal conductivity, but also eliminates several device uncertainties that may contribute an additional 17% error in a measurement. The method also enables local temperature measurements, revealing nanoscale structural variations unfound by SEM. The high accuracy of the technique would make standardization of nanoscale thermal transport measurement possible.

Published under an exclusive license by AIP Publishing. <https://doi.org/10.1063/5.0201873>

Since the introduction of micro-thermal bridges as thermal conductivity measurement platforms for individual one-dimensional nanomaterials,^{1,2} a plethora of interesting phenomena have been discovered. For example, the thermal conductivity of Si nanowires can be tuned via surface scatterings of phonons,^{3,4} reducing it beyond the Casimir limit.⁵ On the other hand, the thermal conductivity of nylon nanofibers can be enhanced by three orders of magnitudes via low-temperature annealing. In addition, anomalous violations of the Wiedemann–Franz law are discovered,⁶ featuring possible non-Fermi liquid behaviors. Furthermore, the thermal conductivities of various nanowires,^{7–13} nanotubes,^{7,14} and graphene ribbons display superdiffusive thermal transport phenomena.¹⁵ Recently, a remarkable enhancement of thermal conductivity has been observed in SiC nanowires with gold coatings on the ends, attributing to the contribution from surface phonon polaritons.¹⁶ However, because all experiments mentioned earlier are based on a two-probe method employing micro-thermal

bridges, the measured total resistance (R_{total}) of the system unavoidably consists of the following terms:

$$R_{\text{total}} = R_{c,\text{left}} + R_{\text{sample}} + R_{c,\text{right}}, \quad (1)$$

where $R_{c,\text{left}}$ and $R_{c,\text{right}}$ are the contact resistance of the left and right probe, respectively. Thus, even though the precision of the micro-thermal bridge measurement can reach pWK^{-1} regime at room temperature,¹⁷ the presence of non-zero $R_{c,\text{left}}$ or $R_{c,\text{right}}$ has always obscured the intrinsic resistance (R_{sample}) and thermal conductivity (κ_{sample}) of the sample to be accurately determined. Many remarkable discoveries mentioned above would be questioned if researchers could not quantitatively address the contributions from $R_{c,\text{left}}$ and $R_{c,\text{right}}$.

For electrical measurement, we have a four-probe method to resolve the problem. In a four-probe configuration, the outer two probes inject/collect electrical current to/from the system, and the inner two probes measure voltage difference across the sample.

The principle of the four-probe method relies on the input impedance of the voltage meter to be much larger than R_{sample} so that insignificant electrical currents can leak into the voltage meter, resulting in negligible contact resistance at the inner probes. The four-probe method can generally be applied to diffusive or ballistic conductors, even though the latter would give $R_{\text{sample}} = 0$ in the four-probe configuration.¹⁸ However, because the thermal conductivities of materials span a much smaller range than electrical conductivities, no probe-based thermometers could exhibit sufficiently good thermal insulation for applying the analogy of the four-probe method to thermal transport measurements.

The two-probe thermal transport measurements employing the micro-thermal bridges are based on the circuit model shown in Fig. 1(a). Here, an investigated sample is anchored across two micro-thermometers, which are usually made of Pt films deposited on suspended SiN_x microbeams (supplementary material, S1). The micro-thermometer can serve as a thermal current sensor. Additionally, because one can apply Joule heating power to raise its temperature, it can also serve as a thermal current source (i.e., a heater). Without loss of generality, we assign the left/right micro-thermometer to serve as a heater/sensor. When a Joule heating is applied to the heater to create a temperature difference across the sample, the temperatures of the heater and the sensor are, respectively, raised above the ambient temperature (T_0) by $T_L = (c_{h,\text{left}}/\alpha_{\text{left}})\Delta R_{\text{left}}$ and $T_R = (c_{s,\text{right}}/\alpha_{\text{right}})\Delta R_{\text{right}}$ (where α_{left} and α_{right} are the temperature coefficient of resistance of the Pt films of the left and the right micro-thermometer, and $c_{h,\text{left}}$ and $c_{s,\text{right}}$ are geometric correction factors that relate the measured resistance change of the left micro-thermometer (ΔR_{left}) and the right micro-thermometer (ΔR_{right}) to the local temperature T_L and T_R where the nanowire is anchored at the heater and sensor, respectively). From Fig. 1(a), the total thermal resistance of the system is obtained using the following relation:

$$\begin{cases} P_R = IV \left(\frac{K_{D,\text{right}} T_R}{K_{D,\text{left}} T_L + K_{D,\text{right}} T_R} \right) = K_{D,\text{right}} T_R \\ \frac{1}{R_{\text{total}}} = \frac{P_R}{T_L - T_R}, \end{cases} \quad (2)$$

where P_R is the heat flux flowing through the sample and detected by the right micro-thermometer, IV is the total Joule heating power,

$K_{D,\text{left}}$ and $K_{D,\text{right}}$ are, respectively, the thermal conductance of the left and the right micro-thermometer.

Many factors in Eq. (2) would prohibit accurate measurements of R_{sample} . First, the two-probe method makes $R_{c,\text{left}}$ and $R_{c,\text{right}}$ inseparable from R_{sample} . Second, relating the measured ΔR_{left} and ΔR_{right} to the local temperature T_L and T_R in a real device based on the circuit model shown in Fig. 1(a) is far from trivial. For example, estimating the $K_{D,\text{left}}$ and $K_{D,\text{right}}$ would be difficult even if a nanowire is anchored at the center of a micro-thermal bridge shown in Fig. 1(b). On the other hand, difficulties in estimating $c_{h,\text{left}}$ and $c_{s,\text{right}}$ may arise when a nanowire's position deviates from the center of a thermal micro-bridge, as depicted in Fig. 1(c) (supplementary material, S2).

Many researchers have made efforts to solve the problem. Repeating a series of two-probe measurements using different nanowires of distinct lengths can be carried out to obtain the length-dependent thermal resistance behavior ($R(x)$).^{8,11-13} The contact thermal resistance is obtained via $R(x \rightarrow 0) = R_{c,\text{left}} + R_{c,\text{right}}$. However, the experimental procedure is inefficient, and it is established on an unjustified assumption that $R_{c,\text{left}} + R_{c,\text{right}}$ remains a constant for different nanowires. On the other hand, a multi-probe method has been introduced to deduce R_c 's from R_{total} 's at distinct sections of the probes.¹⁹⁻²¹ However, the separation of the probes must be larger than micrometers to ensure that the background near-field thermal radiation between nearby probes is negligible. Hsiao *et al.* have employed a nanomanipulator to study $R_{\text{total}}(x)$ of two nanowires in series and assumed the minimum value occurs when the contact thermal resistance between the two nanowires is negligible.⁹ However, $R_{c,\text{left}}$ and $R_{c,\text{right}}$ of the system remain unknown. Recently, intriguing thermal transport phenomena carried by surface phonon-polaritons have been suggested in gold-coated SiC nanowires and SiO₂ nanoribbons using micro-thermal bridges.^{16,22} Pan *et al.* obtain $R(x)$ by repeatedly cutting and transferring the same SiC nanowire to evaluate $R_{c,\text{left}} + R_{c,\text{right}}$.¹⁶ However, it is a time-consuming task, and many failures can be foreseen during the laborious processes.

Alternatively, combining a scanning electron microscope (SEM) with the micro-thermal bridge has facilitated thermal conductance measurements across heterojunctions and interfaces.²³⁻²⁶ Here, the heat currents generated by the electron beam are detected by two independent micro-thermometers at the ends, and $R(x)$ is obtained using the following relation:

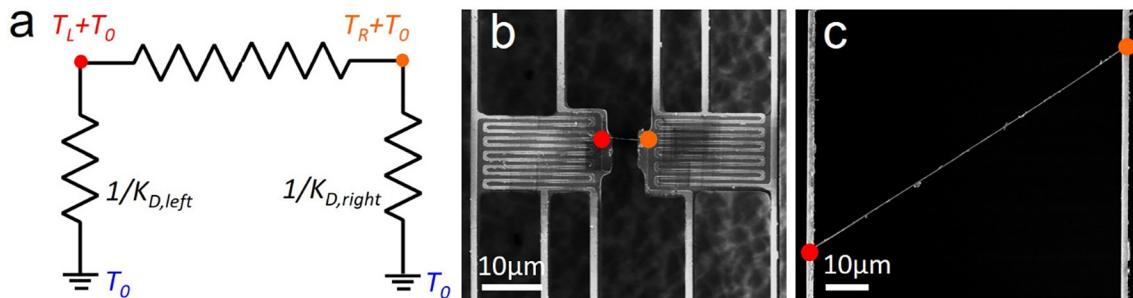


FIG. 1. (a) An equivalent thermal circuit for a micro-thermal bridge. (b) and (c) SEM images of a micro-thermal bridge with a nanowire connected to it. The temperature rises at the ends of a nanowire are denoted as T_L (red dot) and T_R (orange dot), respectively. The thermal resistance of the left and the right micro-thermometer are denoted as $1/K_{D,\text{left}}$ and $1/K_{D,\text{right}}$, respectively. Note that the position and the angle of the investigated nanowire connected to the micro-thermal bridge will affect the effective $K_{D,\text{left}}$, $K_{D,\text{right}}$, $c_{h,\text{left}}$, and $c_{s,\text{right}}$.

$$\begin{cases} T_e = P_{e,L}(R(l-x) + 1/K_{D,left}) = P_{e,R}(R(x) + 1/K_{D,right}), \\ R_{total} = R(x) + R(l-x) \end{cases}, \quad (3)$$

where T_e is the local temperature underneath the electron beam heating, l is the length of the nanowire, $P_{e,L}$ and $P_{e,R}$ are the heat flux flowing collected by the left and right thermometers, respectively. Note that a diffusive sum rule has been imposed in the second equation, which is different from the ballistic sum rule, i.e., $R_{total} \geq (R_{left} R_{right})_{max}$ [where $(R_{left} R_{right})_{max}$ denotes the maximum value of the set $(R_{left} R_{right})$ of two ballistic conductors connected in series].⁸ Because the electron beam heating method is capable of reaching ~ 20 nm resolution,²³ coinciding with the length scale of phonon mean free path of many materials, the diffusive sum rule implicitly used in the works is exclusively applicable to diffusive conductors only.^{19–21,23}

Here, we introduce a universal three-probe thermal transport measurement method to solve the problem. The method consists of three steps. First, the experimental procedure employed for the two-probe measurement expressed in Eq. (2) is conducted to set the reference zeros of the left micro-thermometer (i.e., $P_L + P_R = 0$), as shown in Fig. 2(a). Second, the thermal current ($P_e = P_{e,L} + P_{e,R}$) injected by an electron beam at position x , respectively, raises the left and the right micro-thermometer to $T_{e,L}$ and $T_{e,R}$ above the ambient temperature T_0 , as shown in Fig. 2(b). Third, the temperature of the left micro-thermometer is raised to T'_L at which the thermal current flowing out of it ($-P_R$) balances with the incoming $P_{e,L}$ (i.e., $-P_R + P_{e,L} = 0$), as shown in Fig. 2(c). Based on the zeroth law of thermodynamics, we have $T'_L = T'_e$ (where T'_e is the local temperature at x when T'_L is reached). When the condition is satisfied, P_e would flow to the right micro-thermometer and further raise its temperature to T'_R . We have

$$\begin{cases} T'_e - T'_R = T'_L - T'_R = P_e R(l-x), \\ \frac{T'_L - T'_R}{P_e} = \frac{T_e - T_R}{P_R}. \end{cases} \quad (4)$$

Thus, the zeroth law of thermodynamics is used for determining T'_e and Fourier's law (i.e., heat flux is proportional to the temperature gradient) is employed for obtaining T_e and $R(l-x)$ without imposing any other assumptions associated with diffusive transport.

We now describe the experimental procedures in terms of the directly measured quantities ΔR_{left} vs ΔR_{right} . Following our definition of heat flow, P_L (or ΔR_{right}) becomes more negative when Joule heating is increased at the left in step 1, as illustrated in Fig. 2(d). In step 2, the electron beam heating at x creates an incoming (positive) heat flux, respectively, adding ΔR_{left} and ΔR_{right} to the left and right micro-thermometers, as shown in Fig. 2(e). The total heating power of the electron beam is $P_e = P_{e,L} + P_{e,R}$. In step 3, we repeat step 1 with the presence of the electron beam heating, as shown in Fig. 2(f). The ΔR_{left} vs ΔR_{right} can be converted to T_L vs $(P_L + P_{e,L})$ relations, as described in previous paragraph and shown in Fig. 2(g). Based on the zeroth law of thermodynamics, $T'_L = T'_e$ happens when $P_L + P_{e,L} = -P_R + P_{e,L} = 0$, corresponding to the intersection point denoted in Fig. 2(g). At the same time, $P_R + P_{e,R} = P_e$ is satisfied and all net P_e flows to the right micro-thermometer. We note that both $P_L + P_{e,L} = 0$ and $P_R + P_{e,R} = P_e$ can be used as independent conditions for determining T'_e . Thus, the associated T_e can be obtained by the two independent methods as well. To distinguish, we denote them $T_{e,leftH}$ and $T_{e,rightS}$ determined, respectively, from the left micro-thermometer being used as a heater and the right micro-thermometer serving as a sensor. The procedures described in Figs. 2(a-f) are repeated at different x as well as swapping the heater/sensor roles of the left and right micro-thermometers to obtain $R(x)$. Because the method based on Eq. (3) has

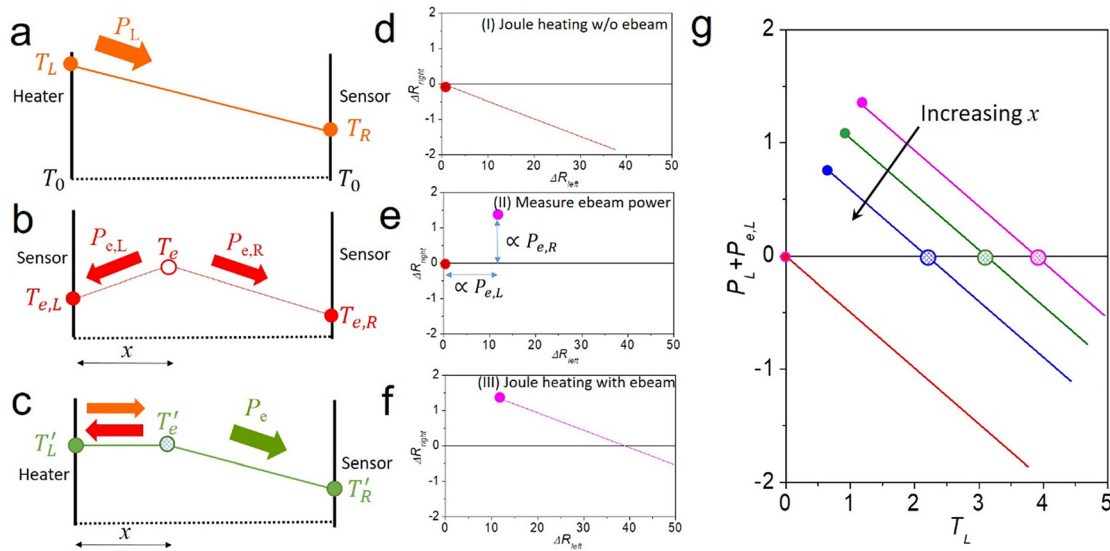


FIG. 2. The universal method of thermal transport measurement. (a) and (d) Step 1, an increasing Joule heating power is applied to the left micro-thermometer and ΔR_{left} vs ΔR_{right} is measured. (b) and (e) Step 2, an electron beam is positioned at x , whose heating power, respectively, flowing to the left [$P_{e,L} = (c_{h,left}/\alpha_{left})\Delta R_{left}$] and the right [$P_{e,R} = (c_{h,right}/\alpha_{right})\Delta R_{right}$] micro-thermometer is measured. (c) and (f) step 3, repeating step 1 while keeping the electron beam heating at x . The arrows denote the flows of thermal currents. (g) The ΔR_{left} vs ΔR_{right} relations are converted to T_L vs $(P_L + P_{e,L})$, and the steps 1–3 are repeated when relocating the electron beam positions. The shaded circles intersecting at $P_L + P_{e,L} = 0$ denote the T_e when the electron beam moves away (i.e., increasing x) from the left micro-thermometer.

employed the simplified diffusive sum rule and the method depicted in Eq. (4) and Fig. 2 roots on a universal thermodynamic law, we name the former “simplified method” and ours as the “universal method.” In addition, applying consistency of the two methods enables us to determine $c_{h,left}$ and $c_{s,right}$ further reducing the uncertainties of κ_{sample} (supplementary material, S3). Moreover, for a diffusive thermal conductor with homogeneous material properties, $T_e(x)$ would be a parabolic curve determined by the variables of $R_{c,left}$, $R_{c,right}$, $K_{D,left}$ and $K_{D,right}$ (supplementary material, S4). The theoretical fitting of $T_e(x)$ will unravel deviations from the homogeneous assumptions at the nanoscale. We will apply these methods to investigate $R(x)$ and $T_e(x)$ of various samples.

Figures 3(a)–3(c) show the SEM image, $R(x)$, $R(l-x)$, $T_{e,left}(x)$, and $T_{e,right}(x)$ of a 200 μm -long SiN_x microbeam with a 30 nm-thick Pt film deposited on it. Here, $R(x)$ displays diffusive conduction, and its $T_e(x)$ shows a parabolic curve for a homogeneous sample. Curiously, $R_{c,left} = 0.023$ MK/W is three times larger than $R_{c,right} = 0.007$ MK/W even though the SiN_x beam and the left/right microthermometer are made of identical materials. Because a focused ion

beam (FIB) has been employed to remove the Pt film near the contacts to ensure electrical insulation between the left and the right microthermometers, we attribute the effect to the dissimilar invasive cutting processes that lead to the finite and different R_c 's. Because samples shown in Figs. 3(b) and S2(e) (supplementary material, S3) are made from the same wafer, we can compare the results to test the precision of our method. Without removing the contributions of $R_{c,left}$ and $R_{c,right}$, the thermal conductivities of Figs. 3(b) and S2(e) would differ by 8%. After removing the contributions of $R_{c,left}$ and $R_{c,right}$, κ_{sample} from the two samples differ by 2% only, demonstrating the high accuracy and precision of our measurements.

Figures 3(d)–3(f) show the SEM image, $R(x)$, $R(l-x)$, $T_{e,left}(x)$, and $T_{e,right}(x)$ of a stoichiometric Si_3N_4 nanowire. Although $R(x)$ displays diffusive behavior with $\kappa_{sample} = 8.4$ W m⁻¹ K⁻¹, $T_e(x)$ strongly deviates from the expected parabolic shape and shows a pronounced peak at the center of the nanowire. From the SEM image shown in Fig. 3(d), we find that a nanoparticle is attached at the center of the nanowire, coinciding with the peak in Fig. 3(f). When high-energy electrons interact with a sample, they undergo a stochastic process

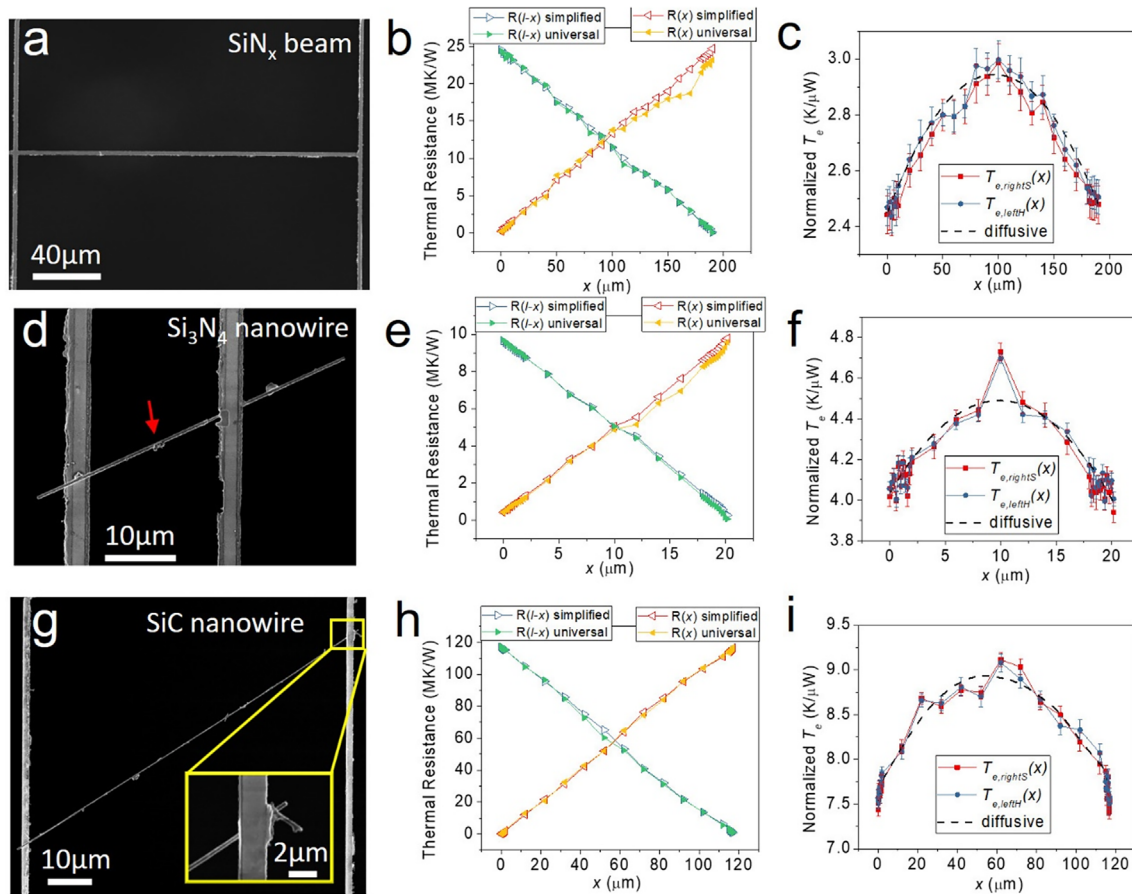


FIG. 3. (Left panels) SEM images, (middle panels) $R(x)$, $R(l-x)$ measured by the two methods, and (right panels) the corresponding $T_{e,left}(x)$ and $T_{e,right}(x)$. (a)–(c) a 200 μm -long SiN_x microbeam, which is made by the same wafer as the similar microbeam shown in Fig. 3(c). (d)–(f) a stoichiometric Si_3N_4 nanowire. Note that a nanoparticle (denoted by a red arrow) is attached to it and contributes to the peak of $T_e(x)$. (g)–(i) a 3C-SiC nanowire, where the contact of the nanowire was loosely connected to the right microthermometer and then significantly improved after carbon deposition [shown in the inset of (g)]. The theoretical $T_e(x)$ of a homogeneous diffusive thermal conductor is shown as a dashed curve in (c), (f), and (i).

within a penetration depth and dissipate their energy into heat.²⁷ Under a 5 kV electron beam, the penetration depth is estimated to be 390 nm for Si₃N₄ (supplementary material, S5), which is smaller than the diameter ($D = 500$ nm) of the nanowire. Thus, the peak can be attributed to the enhanced cross-sectional interaction between the electron beam and the nanoparticle.

Figures 3(g)–3(i) show the SEM image, $R(x)$, $R(l-x)$, $T_{e, \text{left}}(x)$, and $T_{e, \text{right}}(x)$ of a 3C–SiC nanowire. The $R(x)$ and T_e display diffusive thermal conduction with $\kappa_{\text{sample}} = 15.5 \text{ W m}^{-1} \text{ K}^{-1}$, which is comparable to similar 3C–SiC nanowires ($\kappa_{\text{sample}} = 14.7\text{--}28.7 \text{ W m}^{-1} \text{ K}^{-1}$) measured by Pan *et al.*¹⁶ Because the nanowire diameter ($D = 255$ nm)

investigated here is much larger than those ($D = 47\text{--}77$ nm) measured by Pan *et al.*, the result may suggest that surface scatterings of phonons are not significant in Pan *et al.*'s samples. Note that $R_{c, \text{left}} = 0.251$ and $R_{c, \text{right}} = 7.29$ MK/W are found to be significantly reduced after employing electron-beam-induced carbon deposition at both contacts, resulting in $R_{c, \text{left}} = 0.083$ and $R_{c, \text{right}} = 0.818$ MK/W, respectively, shown in Fig. 3(i). The capability to distinguish $R_{c, \text{left}}$ and $R_{c, \text{right}}$ and to quantify their variations has never been reported in previous works.

Figures 4(a)–4(l) show the SEM images, $R(x)$, and $T_e(x)$ of four Ni nanowires. Interestingly, although the Ni nanowires are synthesized

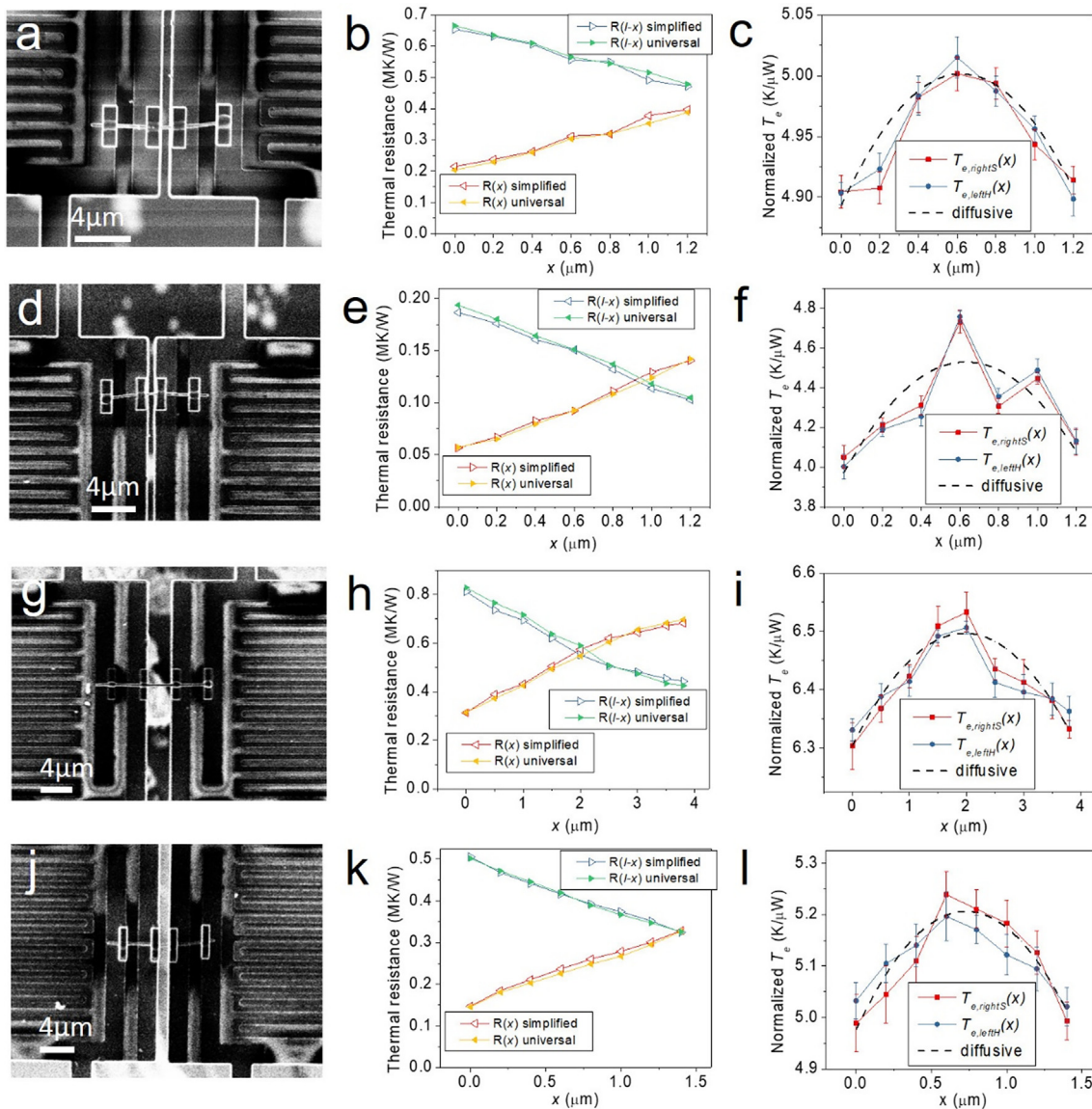


FIG. 4. (Left panels) SEM images, (middle panels) $R(x)$, $R(l-x)$ measured by the two methods, and (right panels) the corresponding $T_{e, \text{left}}(x)$ and $T_{e, \text{right}}(x)$. (a)–(c) a 1.2 μm -long, $D = 300$ nm Ni nanowire. (d)–(f) a 1.2 μm -long, $D = 680$ nm Ni nanowire. (g)–(i) a 3.8 μm -long, $D = 450$ nm Ni nanowire. (j)–(l) a 1.4 μm -long, $D = 400$ nm Ni nanowire. After removing the contact thermal resistance, κ_{sample} are found to be 73.1, 39.4, 64.8, and 61.4 $\text{W m}^{-1} \text{ K}^{-1}$, respectively. The theoretical $T_e(x)$ of a homogeneous diffusive thermal conductor is shown as a dashed curve in (c), (f), (i), and (l).

and collected from the same batch, their measured quantities display distinct characteristics. For example, κ_{sample} varies from 39.4 to 73.1 W m⁻¹ K⁻¹, which is 40%–75% of the thermal conductivity of bulk Ni. In addition, no simple correlation is found between κ_{sample} and the nanowires' diameters. In addition, $R_{c,\text{left}}$ and $R_{c,\text{right}}$ vary from 0.056 to 0.443 MK/W, and the associated interfacial thermal conductance $G_c = 1/(AR_c)$, (where A is the physical contact area estimated from their SEM images) also changes from 3.58 to 18.76 MW/m²K even though the same Pt/C deposition processes have been applied to the four samples. From the data of $R_{c,\text{left}}$, $R_{c,\text{right}}$, and A , we could not find a simple relationship between them, suggesting that factors affecting R_c 's are more complex in realistic situations. Curiously, $R(x)$ of all samples display diffusive transport except for Ni#3, whose $R(x)$ and $R(L-x)$ show deviations from a linear relationship starting at $x = 2.5 \mu\text{m}$. After a closer inspection of the SEM image of Ni#3, we find that the deviation can be attributed to the diameter increase at $x > 2.5 \mu\text{m}$. Interestingly, $T_c(x)$ of Ni#2 and Ni#3 show deviations from the expected parabolic curve, yet no pronounced structural variations are found in their SEM images. From their similarities to the shape of $T_c(x)$ in Fig. 3(f), we speculate that they could originate from enhanced thermal absorption of nanoparticles hidden beneath the Ni#2 and Ni#3 nanowires. The results demonstrate that oxidation, grain boundaries, nanowire diameters, surface structures, and contact deposition processes could all affect κ_{sample} of metallic nanowires,²⁸ and one should not naively anticipate that different nanomaterials would display identical thermal transport properties. We have summarized our results in a Table (supplementary material, S6). From our data, we find that $R_{c,\text{left}} + R_{c,\text{right}}$ may contribute more than 73% of R_{total} which would introduce an error of more than 270% to κ_{sample} . Moreover, the uncertainties of geometric factors, if simply using parameters provided by simulations, may add an additional 17% error to a measurement (supplementary material, S2, S3, and S6).

For non-diffusive thermal conductors, the assumption imposed by the simplified method may not hold, and disagreements between the two methods would indicate interesting phenomena. Disagreements may also happen when the thermal radiation loss of a nanowire becomes significant. Nevertheless, many extraordinary phenomena associated with the thermal transport of individual nanowires have been reported since the introduction of the two-probe thermal conductivity measurement employing micro-thermal bridges. Yet the method is constantly plagued by the difficulties of quantifying the contributions from the contacts. The universal three-probe method introduced here would make standardization of nanoscale thermal transport measurements possible.

See the supplementary material for details of experimental methods and analyses.

This work was supported by the Ministry of Science and Technology of Taiwan (Nos. MOST 111-2112-M-002-043-MY3, 110-2119-M-002-010-MBK, and NSTC 112-2223-E-002-013) and the Center of Atomic Initiative for New Materials, National Taiwan University, from the Featured Areas Research Center Program within the framework of the Higher Education Sprout Project by the Ministry of Education in Taiwan (No. 108L9008).

AUTHOR DECLARATIONS

Conflict of Interest

The authors have no conflicts to disclose.

Author Contributions

Po-Yen Huang: Data curation (equal); Formal analysis (equal); Investigation (equal). **Tzu-Kan Hsiao:** Data curation (equal); Formal analysis (equal); Investigation (equal); Methodology (equal); Software (equal). **Jiun-Hung Yi:** Investigation (equal); Resources (equal). **Bo-Yi Chen:** Data curation (equal); Investigation (equal); Resources (equal). **Yu-Cheng Chiu:** Data curation (equal); Formal analysis (equal). **I-Ling Chang:** Formal analysis (equal); Resources (equal); Software (equal); Supervision (equal). **Tien-Kan Chung:** Investigation (equal); Resources (equal). **Ming-Chang Lu:** Formal analysis (equal); Funding acquisition (equal); Investigation (equal); Project administration (equal); Resources (equal); Supervision (equal). **Chih-Wei Chang:** Conceptualization (equal); Data curation (equal); Formal analysis (equal); Funding acquisition (equal); Project administration (equal); Resources (equal); Supervision (equal); Validation (equal); Writing – original draft (equal); Writing – review & editing (equal).

DATA AVAILABILITY

The data that support the findings of this study are available from the corresponding authors upon reasonable request.

REFERENCES

- L. Shi, D. Y. Li, C. H. Yu, W. Y. Jang, D. Kim, Z. Yao, P. Kim, and A. Majumdar, "Measuring thermal and thermoelectric properties of one-dimensional nanostructures using a microfabricated device," *J. Heat Transfer* **125**, 881–888 (2003).
- P. Kim, L. Shi, A. Majumdar, and P. L. McEuen, "Thermal transport measurements of individual multiwalled nanotubes," *Phys. Rev. Lett.* **87**, 215502 (2001).
- D. Y. Li, Y. Y. Wu, P. Kim, L. Shi, P. D. Yang, and A. Majumdar, "Thermal conductivity of individual silicon nanowires," *Appl. Phys. Lett.* **83**, 2934–2936 (2003).
- R. K. Chen, A. I. Hochbaum, P. Murphy, J. Moore, P. D. Yang, and A. Majumdar, "Thermal conductance of thin silicon nanowires," *Phys. Rev. Lett.* **101**, 105501 (2008).
- J. W. Lim, K. Hippalgaonkar, S. C. Andrews, A. Majumdar, and P. D. Yang, "Quantifying surface roughness effects on phonon transport in silicon nanowires," *Nano Lett.* **12**, 2475–2482 (2012).
- S. Lee, K. Hippalgaonkar, F. Yang, J. W. Hong, C. Ko, J. Suh, K. Liu, K. Wang, J. J. Urban, X. Zhang, C. Dames, S. A. Hartnoll, O. Delaire, and J. Q. Wu, "Anomalously low electronic thermal conductivity in metallic vanadium dioxide," *Science* **355**, 371 (2017).
- C. W. Chang, D. Okawa, H. Garcia, A. Majumdar, and A. Zettl, "Breakdown of Fourier's law in nanotube thermal conductors," *Phys. Rev. Lett.* **101**, 075903 (2008).
- T. K. Hsiao, H. K. Chang, S. C. Liou, M. W. Chu, S. C. Lee, and C. W. Chang, "Observation of room temperature ballistic thermal conduction persisting over 8.3 micrometers in SiGe nanowires," *Nat. Nanotechnol.* **8**, 534–538 (2013).
- T. K. Hsiao, B. W. Huang, H. K. Chang, S. C. Liou, M. W. Chu, S. C. Lee, and C. W. Chang, "Micron-scale ballistic thermal conduction and suppressed thermal conductivity in heterogeneously-interfaced nanowires," *Phys. Rev. B* **91**, 035406 (2015).
- R. Anufriev, S. Gluchko, S. Volz, and M. Nomura, "Quasi-ballistic heat conduction due to Lévy phonon flights in silicon nanowires," *ACS Nano* **12**, 11928–11935 (2018).

- ¹¹D. Vakulov, S. Gireesan, M. Y. Swinkels, R. Chavez, T. Vogelaar, P. Torres, A. Campo, M. De Luca, M. A. Verheijen, S. Koelling, L. Gagliano, J. E. M. Haverkort, F. X. Alvarez, P. A. Bobbert, I. Zardo, and E. P. A. M. Bakkers, “Ballistic phonons in ultrathin nanowires,” *Nano Lett.* **20**, 2703–2709 (2020).
- ¹²Q. Zhang, C. H. Liu, X. Liu, J. Y. Liu, Z. G. Cui, Y. Zhang, L. Yang, Y. Zhao, T. T. Xu, Y. F. Chen, J. Wei, Z. C. Mao, and D. Y. Li, “Thermal transport in quasi-1D van der Waals crystal $\text{Ta}_2\text{Pd}_3\text{Se}_8$ nanowires: Size and length dependence,” *ACS Nano* **12**, 2634–2642 (2018).
- ¹³L. Yang, Y. Tao, Y. L. Zhu, M. Akter, K. Wang, Z. L. Pan, Y. Zhao, Q. Zhang, Y. Q. Xu, R. K. Chen, T. T. Xu, Y. F. Chen, Z. Q. Mao, and D. Y. Li, “Observation of superdiffusive phonon transport in aligned atomic chains,” *Nat. Nanotechnol.* **16**, 764 (2021).
- ¹⁴V. Lee, C. H. Wu, Z. X. Lou, W. L. Lee, and C. W. Chang, “Divergent and ultrahigh thermal conductivity in millimeter-long nanotubes,” *Phys. Rev. Lett.* **118**, 135901 (2017).
- ¹⁵X. F. Xu, L. F. C. Pereira, Y. Wang, J. Wu, K. W. Zhang, X. M. Zhao, S. Bae, C. T. Bui, R. G. Xie, J. T. L. Thong, B. H. Hong, K. P. Loh, D. Donadio, B. W. Li, and B. Özyilmaz, “Length-dependent thermal conductivity in suspended single-layer graphene,” *Nat. Commun.* **5**, 3689 (2014).
- ¹⁶Z. Pan, G. Lu, X. Li, J. R. McBride, R. Juneja, M. Long, L. Lindsay, J. D. Caldwell, and D. Li, “Remarkable heat conduction mediated by non-equilibrium phonon polaritons,” *Nature* **623**, 307–312 (2023).
- ¹⁷J. L. Zheng, M. C. Wingert, E. Dechaumphai, and R. K. Chen, “Sub-picowatt/kelvin resistive thermometry for probing nanoscale thermal transport,” *Rev. Sci. Instrum.* **84**, 114901 (2013).
- ¹⁸R. de Picciotto, H. L. Stormer, L. N. Pfeiffer, K. W. Baldwin, and K. W. West, “Four-terminal resistance of a ballistic quantum wire,” *Nature* **411**, 51–54 (2001).
- ¹⁹J. Kim, E. Ou, D. P. Sellan, and L. Shi, “A four-probe thermal transport measurement method for nanostructures,” *Rev. Sci. Instrum.* **86**, 044901 (2015).
- ²⁰B. Smith, G. Fleming, K. D. Parrish, F. Wen, E. Fleming, K. Jarvis, E. Tutuc, A. J. H. McGaughey, and L. Shi, “Mean free path suppression of low-frequency phonons in SiGe nanowires,” *Nano Lett.* **20**, 8384–8391 (2020).
- ²¹Q. R. Jia, Y. Y. Zhou, X. Li, L. Lindsay, and L. Shi, “Differential multi-probe thermal transport measurements of multi-walled carbon nanotubes grown by chemical vapor deposition,” *Int. J. Heat Mass Transfer* **216**, 124535 (2023).
- ²²Y. Pei, L. Chen, W. Jeon, Z. Liu, and R. Chen, “Low-dimensional heat conduction in surface phonon polariton waveguide,” *Nat. Commun.* **14**, 8242 (2023).
- ²³D. Liu, R. G. Xie, N. Yang, B. W. Li, and J. T. L. Thong, “Profiling nanowire thermal resistance with a spatial resolution of nanometers,” *Nano Lett.* **14**, 806–812 (2014).
- ²⁴Y. S. Zhao, D. Liu, J. Chen, L. Y. Zhu, A. Belianinov, O. S. Ovcinnikova, R. R. Unocic, M. J. Burch, S. Kim, H. F. Hao, D. S. Pickard, B. W. Li, and J. T. L. Thong, “Engineering the thermal conductivity along an individual silicon nanowire by selective helium ion irradiation,” *Nat. Commun.* **8**, 15919 (2017).
- ²⁵A. Aiyiti, X. Bai, J. Wu, X. F. Xu, and B. W. Li, “Measuring the thermal conductivity and interfacial thermal resistance of suspended MoS_2 using electron beam self-heating technique,” *Sci. Bull.* **63**, 452–458 (2018).
- ²⁶Y. S. Zhao, X. J. Liu, A. Rath, J. Wu, B. W. Li, W. X. Zhou, G. F. Xie, G. Zhang, and J. T. L. Thong, “Probing thermal transport across amorphous region embedded in a single crystalline silicon nanowire,” *Sci. Rep.* **10**, 821 (2020).
- ²⁷C. C. Lin, S. M. Wang, B. Y. Chen, C. H. Chi, I. L. Chang, and C. W. Chang, “Scanning electron thermal absorbance microscopy for light element detection and atomic number analysis,” *Nano Lett.* **22**, 2667–2673 (2022).
- ²⁸W. T. Peng, F. R. Chen, and M. C. Lu, “Thermal conductivity and electrical resistivity of single copper nanowires,” *Phys. Chem. Chem. Phys.* **23**, 20359–20364 (2021).

Supplementary Material

A three-probe method for accurate nanoscale thermal transport measurements

Po-Yen Huang,^{1,2} Tzu-Kan Hsiao,³ Jiun-Hung Yi,² Bo-Yi Chen,¹ Yu-Cheng Chiu,^{1,4} I-Ling Chang,⁴ Tien-Kan Chung,⁵ Ming-Chang Lu,^{2,6*} and Chih-Wei Chang^{1,7*}

¹ Center for Condensed Matter Sciences, National Taiwan University, Taipei 10617, Taiwan

² Department of Mechanical Engineering, National Taiwan University, Taiwan 10617, Taiwan

³ Department of Physics, National Tsing Hua University, Hsinchu 30013, Taiwan

⁴ Department of Mechanical Engineering, National Cheng Kung University, Tainan 70101, Taiwan

⁵ Department of Mechanical Engineering, National Chiao Tung University, Hsinchu 30010, Taiwan

⁶ Graduate School of Advanced Technology, National Taiwan University, Taipei 10617, Taiwan

⁷ Center of Atomic Initiative for New Materials, National Taiwan University, Taipei, 10617, Taiwan

S1. Device fabrication and sample preparation

The fabrication of the thermal micro-bridges initiated with the preparation of a 400-nm-thick low-stress SiN_x film on both sides of a Si substrate through low-pressure chemical vapor deposition (LPCVD). Subsequently, the wafer underwent dehydration baking at 125°C for 30 minutes. A positive photoresist layer (Shipley S1813) was then spin-coated onto the Si wafer at 4000 rpm for 45 seconds, followed by a soft-bake at 120°C for 90 seconds. The wafer was exposed using an MA6 SUSS mask aligner in hard contact mode and developed for 30 seconds in developer MF-319 to imprint the desired pattern onto the wafer. Subsequently, a thin film of Cr(5nm)/Pt(30nm) was deposited using electron beam evaporation, followed by a standard lift-off procedure. Another round of lithography was employed to define the top-side SiN_x pattern and backside window pattern. The exposed SiN_x film regions on both sides of the wafer were etched using a PlasmaPro system 100 RIE (Oxford Instruments) with CHF₃/O₂ Chemistry. Following the SiN_x film etching, tetramethylammonium hydroxide (TMAH) was utilized to etch the exposed Si regions, leading to the release of suspended SiN_x beams as the underlying Si was selectively etched away.

The SiC nanoparticles and nanowires were purchased from Novarials (Catalog

Number: NovaWire-SiC-100-RD). The Ni nanowires were made using anodic aluminum oxide (AAO) as a template and employed electron beam evaporation to deposit a 300nm thick Ni layer as the seed layer for electroplating processes. Then the AAO was removed by KOH. The detailed procedures can be found in Sadin *et al.*¹

S2. $c_{h,left}$, $c_{s,right}$ suggested by simulation

Following Eq. (2) in the main text, the total thermal conductance of the system can be rewritten as:

$$\frac{1}{R_{total}} = \frac{VI}{T_L - T_R} \left(\frac{K_{D,right} T_R}{K_{D,left} T_L + K_{D,right} T_R} \right) = \frac{K_{D,right}}{T_L/T_R - 1} \quad (S1)$$

where IV is the total Joule heating power, $K_{D,left}$ and $K_{D,right}$ are respectively the thermal conductance of the left and the right micro-thermometer. Moreover, $T_L = (c_{h,left}/\alpha_{left})\Delta R_{left}$ and $T_R = (c_{s,right}/\alpha_{right})\Delta R_{right}$, where α_{left} and α_{right} are the temperature coefficient of resistance of the Pt film films of the left and the right micro-thermometer, and $c_{h,left}$ and $c_{s,right}$ are geometric correction factors that relate the measured resistance change of the left micro-thermometer (ΔR_{left}) and the right micro-thermometer (ΔR_{right}) to the local temperature T_L and T_R where the nanowire is anchored at the left micro-thermometer (the default heater) and the right micro-thermometer (the default sensor), respectively. As mentioned in the main text, we can make α_{left} and α_{right} be absorbed in the new dimensionless fitting parameter $c_{s,right}/c_{h,left}$. Here we employ COMSOL multiphysics simulation and Eq. (S1) to read out the local temperatures (T_L , T_R) at the ends of a nanowire as well as the simulated average temperatures ($\Delta R_{left}/\alpha_{left}$, $\Delta R_{right}/\alpha_{right}$) when the left/right micro-thermometer is used as a heater/sensor. Their ratios would determine ($c_{h,left}$, $c_{s,right}$). Thus, we may see how ($c_{h,left}$, $c_{s,right}$) change for different experimental configurations. For the COMSOL simulation. the thermal conductivity of Si_3N_4 is $\kappa=10 \text{ Wm}^{-1}\text{K}^{-1}$. Thermal insulation is set as the boundary condition for all Si_3N_4 beams except the ends where they are connected to a heat sink of 300K.

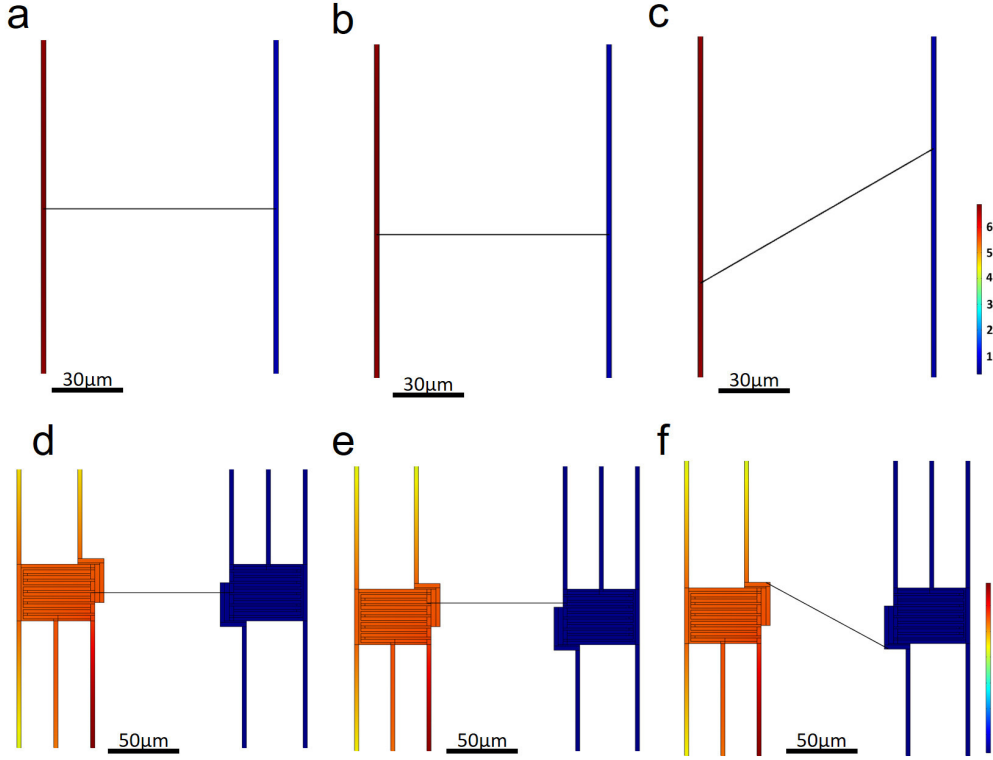


Fig. S1. Simulated temperature distribution of a 200nm wide Si_3N_4 nanowire with $\kappa_{\text{sample}} = 10 \text{ Wm}^{-1}\text{K}^{-1}$ anchored (a, c) at the center, (b, d) off-centered, and (c, f) at angle oblique angle on a pair of micro-thermometers made by (a-c) 800 μm -long Si_3N_4 beams with 100nm-thick Pt films on it. (d-f) Si_3N_4 pads with 100nm-thick patterned Pt films on it. We use line average to read the simulated $\Delta R_{\text{left}}/\alpha_{\text{left}}$ and $\Delta R_{\text{right}}/\alpha_{\text{right}}$. The local temperature T_L and T_R are obtained from the ends of nanowire is anchored at the ends of the heater and the sensor, respectively.

Figures S1(a-c) display the simulated temperature map of a 200nm wide Si_3N_4 nanowire with $\kappa_{\text{sample}} = 10 \text{ Wm}^{-1}\text{K}^{-1}$ anchored at the center, off-centered, and at an oblique angle of a pair of micro-thermometers made of 800 μm -long Si_3N_4 beams with 100nm-thick Pt films on it. To correctly give κ_{sample} , the $(c_{\text{h,left}}, c_{\text{s,right}})$ are found to be (1.47, 1.00), (1.47, 1.00), and (1.46, 1.00), respectively. Thus, $c_{\text{s,right}}/c_{\text{h,left}}=0.68$ is suggested by the simulation for devices like Fig. S1(a-c).

Figures S1(d-f) show the simulated temperature map of a 200nm wide Si_3N_4 nanowire with $\kappa_{\text{sample}} = 10 \text{ Wm}^{-1}\text{K}^{-1}$ anchored at the center, off-centered, and at an oblique angle of a pair of micro-thermometers made of Si_3N_4 pads with 100nm-thick patterned Pt films on it. The $(c_{\text{h,left}}, c_{\text{s,right}})$ are found to be (1.006, 1.026), (1.000, 1.044), and (0.995, 1.079), respectively. Notably, if two-probe measurements are employed for measuring $\Delta R_{\text{left}}/\alpha_{\text{left}}$ and $\Delta R_{\text{right}}/\alpha_{\text{right}}$, $(c_{\text{h,left}}, c_{\text{s,right}})$ becomes (1.215, 1.513), (1.237, 1.531), and (1.203, 1.594), respectively. Thus, $c_{\text{s,right}}/c_{\text{h,left}}=1.24$ is suggested by the

simulation for devices like Fig. S1(d-f).

It should be noted that when one employs simulations to obtain the above parameters, the following assumptions are unavoidable: (i) the heater and the sensor are made of uniform beams with homogeneous material properties, (ii) the left and the right micro-thermometers are identical. (iii) the micro-thermometers are free from surface contaminations. Thus, in addition to the unknown $R_{c,left}$ and $R_{c,right}$, many unjustified assumptions imposed by the two-probe thermal transport measurement may prohibited accurate determination of R_{sample} .

S3. Fitting processes for $c_{h,left}$ and $c_{s,right}$

To illustrate how the fitting process works, we first note that the first equation in Eq. (2) in the main text suggests that $K_{D,right}T_R$ is a fraction of IV and the ratio $(c_{s,right}\alpha_{left})/(c_{h,left}\alpha_{right})$ is sufficient to determine R_{total} . Thus, we may let α_{left} and α_{right} be absorbed in the new dimensionless fitting parameter $c_{s,right}/c_{h,left}$. Figures S2(a & b) show the results of $R(x)$, $R(l-x)$, $T_{e,left}H(x)$, and $T_{e,right}S(x)$ of a 50 μ m-long SiN_x beam with a 30nm-thick Pt film deposited on it. Given the initial fitting parameters: $c_{s,right}/c_{h,left}=0.667$, $K_{D,left}=1\times 10^{-6}$ W/K, and $K_{D,right}=1\times 10^{-6}$ W/K, Figs. S2(a & b) show that both methods give $R(x)$ and $R(L-x)$ to be linearly increased with length, suggesting diffusive thermal conduction. In general, we find that the fitting parameters do not affect the observed diffusive behavior even though the values in the y-axis can be rescaled. As shown in Fig. S2(c & d), we then vary the fitting parameters until they give consistent results. The multiple data from $R(x)$, $R(L-x)$, $T_{e,left}H(x)$, and $T_{e,right}S(x)$ allow us to find a unique set of fitting parameters: $c_{s,right}/c_{h,left}=0.6$, $K_{D,left}=1.45\times 10^{-6}$ W/K, and $K_{D,right}=1.5\times 10^{-6}$ W/K. From the final result shown in Fig. S2(e), we can read $R_{c,left}=R(x \rightarrow 0)=0.016$ MK/W and $R_{c,right}=R(l-x \rightarrow 0)=0.029$ MK/W. In addition, both methods also give consistent results of $T_{e,left}H(x)$ and $T_{e,right}S(x)$, as displayed in Fig. 3(f). We note that for a diffusive thermal conductor with homogeneous material properties, $T_e(x)$ would be a parabolic curve determined by the variables of $R_{c,left}$, $R_{c,right}$, $K_{D,left}$, and $K_{D,right}$ (see supplemental material S4). We have inputted the parameters obtained above and found the theoretical curve gives a good fit to the experimental result, as shown in Fig. 3(f). The result suggests that the sample is a diffusive conductor with homogenous material properties and its $\kappa_{sample}=9.7$ Wm⁻¹K⁻¹.

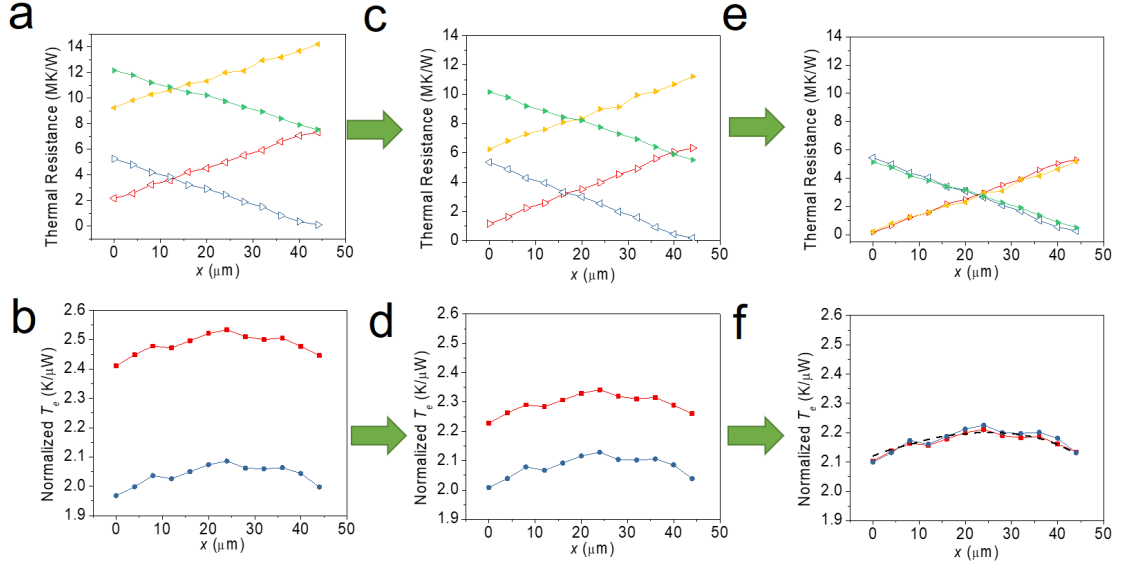


Fig. S2. Fitting processes for obtaining consistent $R(x)$ (left triangles), $R(l-x)$ (right triangles) measured by the simplified method (open symbols) and the universal method (solid symbols), and the corresponding $T_{e,left}(x)$ (dark blue) and $T_{e,right}(x)$ (red) of a SiN_x beam. (a, b) Using initial parameters $c_{s,right}/c_{h,left}=0.667$, $K_{D,left}=1\times 10^{-6}$ W/K, and $K_{D,right}=1\times 10^{-6}$ W/K. (c, d) Using $c_{s,right}/c_{h,left}=0.6$, $K_{D,left}=1.2\times 10^{-6}$ W/K, and $K_{D,right}=1.2\times 10^{-6}$ W/K. (e, f) Consistent results are obtained using $c_{s,right}/c_{h,left}=0.6$, $K_{D,left}=1.45\times 10^{-6}$ W/K, and $K_{D,right}=1.5\times 10^{-6}$ W/K. The theoretical $T_e(x)$ of a homogeneous diffusive thermal conductor is shown as a dashed curve in (f).

S4. T_e of a diffusive conductor

In this section, we will derive the temperature rise ($T_e(x)$) of a diffusive thermal conductor anchored across a micro-thermal bridge when it is heated by an electron beam at x .

Equation (3) of the main text can be rewritten as:

$$(P_e - P_{e,R})(R_{total} - \alpha x + 1/K_{D,left}) = P_{e,R}(1/K_{D,right} + \alpha x)$$

Note that the diffusive condition has been imposed here, i.e. $R(x)=\alpha x$. In addition, $R_{c,left}$ and $R_{c,right}$ can be respectively absorbed into $1/K_{D,left}$ and $1/K_{D,right}$ without affecting the result. Thus we have

$$T_e = (1/K_{D,right} + \alpha x) \left[\frac{P_e(R_{total} - \alpha x + 1/K_{D,left})}{R_{total} + 1/K_{D,left} + 1/K_{D,right}} \right]$$

After rearranging

$$\frac{T_e}{P_e} = \frac{-\alpha^2 x^2 + \alpha(R_{total} + 1/K_{D,left} - 1/K_{D,right})x + R_{total}/K_{D,right} + 1/K_{D,right}K_{D,left}}{R_{total} + 1/K_{D,left} + 1/K_{D,right}}$$

From the above equation, it can be concluded that the normalized T_e is a concave parabolic curve with the maximum value occurring at $x = \frac{R_{total} + 1/K_{D,left} - 1/K_{D,right}}{2\alpha}$. If

the thermal conductance of both sides are the same, the maximum occurs at the center of the nanowire, i.e. $x=l/2$. It can be further proved that the normalized T_e is invariant when swapping the labels of $K_{D,left}$ and $K_{D,right}$.

S5. Simulated penetration depth of a 5KV electron beam

The penetration depth of an electron beam to Si_3N_4 is simulated using the CASINO Monte Carlo program (Version 3.3.0.4) using the MONSEL Defaults model.² The model incorporates the Browning approach for calculating the Mott elastic scattering cross-section and the Joy and Luo model,^{3,4} which has been further modified by Lowney⁵ to calculate inelastic scattering energy loss (dE/dS). Based on previous studies, the simulation has been verified to give good agreements with experimental results.^{6,7} We input 100,000 electrons under acceleration voltages $V_{acc} = 5$ KV and see the absorbance (A) for different thickness of Si_3N_4 .

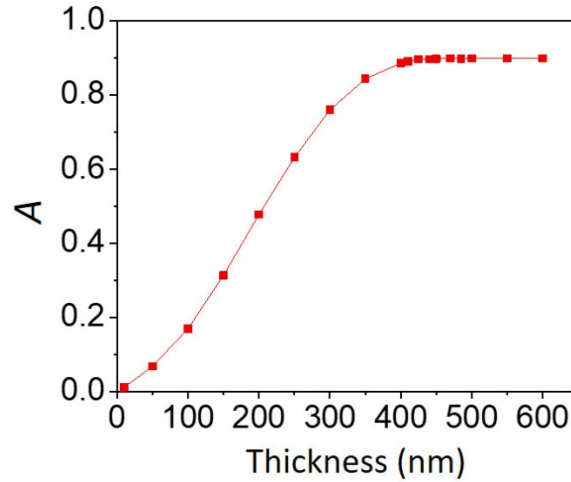


Fig. S3. Simulated thickness vs. absorbance (A) of a Si_3N_4 film under $V_{acc} = 5$ KV. The penetration depth is found to be 390nm.

We vary the thickness of a Si_3N_4 film to investigate its absorbance (A). As shown in Fig. S3, A would monotonically increase when the thickness increases and saturates at a constant value, indicating zero electron transmission. From Fig. S3, we estimate the penetration depth of Si_3N_4 under $V_{acc} = 5$ KV is 390nm. The result explains the observed peak of $T_{e,leftH}(x)$ (dark blue) and $T_{e,rightS}(x)$ in Fig. 3(f) of the main text.

S6. Data summary

Table S1. Experimentally measured quantities

Sample	Length (μm)	Diameter (nm)	K_{sample} ($\text{Wm}^{-1}\text{K}^{-1}$)	$R_{c,left}$ (MK/W)	$G_{c,left}$ ($\text{MW}/\text{m}^2\text{K}$)	$R_{c,right}$ (MK/W)	$G_{c,right}$ ($\text{MW}/\text{m}^2\text{K}$)

SiN _x beam1	50	2000 (width) 430 (thickness)	9.7	0.016	86.81	0.029	47.89
SiN _x beam2	200	2000 (width) 430 (thickness)	9.5	0.023	60.39	0.007	198.41
Si ₃ N ₄	20.2	500	8.4	0.421	2.38	0.273	3.66
SiC	117	255	15.5	0.083	23.62	0.818	2.4
Ni #1	1.2	300	73.1	0.22	10.82	0.47	5.07
Ni #2	1.2	680	39.4	0.056	18.76	0.102	10.3
Ni #3	3.8	450	64.8	0.313	5.07	0.443	3.58
Ni #4	1.4	400	61.4	0.147	12.15	0.324	5.51

Table S2. Fitting parameters

Sample	$K_{D,left}$ ($\mu\text{W/K}$)	$K_{D,right}$ ($\mu\text{W/K}$)	$c_{s,right}/c_{h,left}$ (fitted)	$c_{s,right}/c_{h,left}$ (simulation)	Error in R_{total} [1-(simulation/fitted)]
SiN _x beam1	1.45	1.5	0.6	0.68	-13.3%
SiN _x beam2	1.5	1.45	0.71	0.68	4.2%
Si ₃ N ₄	1.8	1.7	0.688	0.68	1.2%
SiC	1.8	2.0	0.581	0.68	-17%
Ni #1	0.84	0.92	1.33	1.24	6.8%
Ni #2	0.88	0.81	1.19	1.24	-4.2%
Ni #3	0.84	0.79	1.27	1.24	2.4%
Ni #4	0.86	0.91	1.22	1.24	-1.6%

Note that two-probe electrical resistance measurements are employed for measuring $T_h=(c_{h,left}/\alpha_{left})\Delta R_{left}$ and $T_s=(c_{s,right}/\alpha_{right})\Delta R_{right}$ of the Ni nanowires.

From Table S2, we find the fitting results suggest $c_{s,right}/c_{h,left}=0.581\sim 0.71$ for devices like Fig. 3(a,d,g) whereas the simulation suggests $c_{s,right}/c_{h,left}=0.68$. Thus, relying on simulation results would lead to an error as large as 17%. In summary, if one employs simulated ($c_{h,left}$, $c_{s,right}$) in Eq. (S1) to determine R_{total} without the going through the fitting process described in S3, the result would introduce 17% (for devices like Fig. S1(a-c)) and 6.8% (for devices like Fig. S1(d-f)) error in obtaining R_{total} using Eq. (2) or (S1), respectively.

References

1. N. U. Saidin, K. K. Ying & I. K. Ng. Anodic Aluminum Oxide Templates for Nickel Nanowires Array Fabrication. *Advanced Materials Research* **364**, 303-307 (2012).
2. H. Demers, N. Poirier-Demers, A. R. Couture, D. Joly, M. Guilmain, N. de Jonge & D. Drouin. Three-Dimensional Electron Microscopy Simulation with the CASINO Monte Carlo Software. *Scanning* **33**, 135-146 (2011).
3. D. C. Joy & S. Luo. An empirical stopping power relationship for low-energy electrons. *Scanning* **11**, 176-180 (1989).
4. R. Browning, T. Z. Li, B. Chui, J. Ye, R. F. W. Pease, Z. Czyzewski & D. C. Joy. Empirical Forms for the Electron-Atom Elastic-Scattering Cross-Sections from 0.1 to 30 Kev. *J. Appl. Phys.* **76**, 2016-2022 (1994).
5. J. R. Lowney. Monte Carlo simulation of scanning electron microscope signals for lithographic metrology. *Scanning* **18**, 301-306 (1996).
6. C. C. Lin, S. M. Wang, B. Y. Chen, C. H. Chi, I. L. Chang & C. W. Chang. Scanning Electron Thermal Absorbance Microscopy for Light Element Detection and Atomic Number Analysis. *Nano Lett.* **22**, 2667-2673 (2022).
7. P. Y. Yuan, J. Y. Wu, D. F. Ogletree, J. J. Urban, C. Dames & Y. B. Ma. Adapting the Electron Beam from SEM as a Quantitative Heating Source for Nanoscale Thermal Metrology. *Nano Lett.* **20**, 3019-3029 (2020).